Fracture mode transitions in brittle coatings on compliant substrates as a function of thickness

Herzl Chai[a] and Brian R. Lawn[b]
Materials Science and Engineering Laboratory, National Institute of Standards and Technology, Gaithersburg, Maryland 20899

(Received 27 January 2004; accepted 5 March 2004)

The fundamentally changing nature of fracture in brittle coatings on compliant substrates with diminishing coating thickness is examined. Attention is focused on cracking induced by concentrated loading with a spherical indenter at the top surface. It is shown that the fracture mode undergoes transitions, from top-surface ring cracking around the contact ("thick-coating" region) to bottom-surface radial cracking at the lower ceramic surface ("intermediate" region) and, finally, back to surface ring cracking ("thin-coating" region). These transitions reflect a progressively changing stress field in the layer structures and highlight the differences in failure mechanism that may be anticipated at the large- and small-scale levels. Simple fracture relations are derived for each mode, expressing critical loads in terms of coating thickness relative to contact or sphere radius, coating strength and coating/substrate modulus mismatch. Data from finite element simulations and contact experiments on model ceramic/polymer bilayer systems are used to validate the basic elements of the analytical relations and to quantify deviations. Implications of the transitional behavior in relation to the strength of brittle coating/film systems are discussed.

I. INTRODUCTION

Brittle coatings are widely used as mechanical and other functional protection for compliant or soft substrates. Such structures are in widespread use, from thick coatings in engineering and biomechanical applications to ultrathin films in advanced devices. They are highly vulnerable to fracture from concentrated loads, specifically to ring cracking outside the contact at the top surface and to radial cracking immediately below the contact at the bottom surface (i.e., coating/substrate interface).[1–20] Which of these competing fracture modes is operative in any given material system depends largely on the coating thickness: ring cracks are most evident at the thickness extremes where contact stresses dominate in either the coating (thick coatings, typically > 1 mm) or the substrate (thin films, typically < 1 μm); radial cracks are evident at intermediate thicknesses where plate flexure stresses dominate. Coating thickness is therefore a critical scaling factor in the failure properties of brittle layer systems. Questions inevitably arise as to how valid it is to extrapolate fracture relations from the macroscopic domain of thick coatings into the submicrometer domain of ultrathin films.

To address the issue of coating thickness, we analyze here the conditions for fracture in model bilayer systems consisting of brittle ceramic coatings on compliant polymeric substrates, in concentrated loading from a spherical indenter at the top surface. Finite element analysis (FEA) is first used to investigate the changing nature of the stress fields as thickness diminishes and to correlate locations of tensile stress maxima with observed cracking modes. Then explicit relations for the critical loads for each cracking mode, based on a simple critical stress condition for fracture, are presented. For this purpose, it is assumed that the stress field remains linear elastic up to the point of fracture. It is also assumed that one or other of the contact or plate flexure fields totally dominates in any given thickness region. As indicated, coating thickness is a principal variable in these relations; other important factors include indenter size, coating strength and/or flaw size, and coating/substrate elastic modulus mismatch. The FEA calculations are used to verify essential features and limitations of the relations, and to help delineate mode transition regions. Some experiments on glass, alumina and yttria-tetragonal-zirconia polycrystal (Y-TZP) coating layers bonded to polycarbonate substrates over a broad range of coating thickness are then conducted to provide a further check on the

[a]Guest scientist, on leave from the Department of Solid Mechanics, Materials and Systems, Faculty of Engineering, Tel Aviv University, Tel Aviv, Israel.
[b]Address all correspondence to this author.
e-mail: brian.lawn@NIST.gov
DOI: 10.1557/JMR.2004.0219

 © 2004 Materials Research Society

explicit critical load relations. It is thereby demonstrated that the analytical relations provide useful lower bounds to the critical loads for fracture over a wide range of coating thicknesses.

II. ANALYSIS

A. Stress fields and crack systems

Consider the bilayer system with brittle coating layer of thickness d and modulus E_c on a relatively thick compliant substrate of modulus E_s shown schematically in Fig. 1. A spherical indenter of radius r is loaded at the top surface at force P over a contact of radius a. In this analysis, the contact field is considered to remain linear elastic prior to crack initiation at a critical load. The crack locations R change with diminishing relative coating thickness d/a[8]: (a) dominant top-surface near-contact ring or cone cracks ($R/a \approx 1$); (b) dominant bottom-surface axial radial cracks ($R/a = 0$) plus secondary top-surface outer ring cracks ($R/a \gg 1$); (c) still dominant but off-axis radial cracks plus inner ring cracks ($R/a \approx 1$); and (d) through-thickness ring cracks ($R/a \approx 1$). Note that all these cracks propagate transversely into the coating. Other fracture modes may exist in specific systems, e.g., delamination at especially weak coating/substrate interfaces, punch-in shear failures in highly anisotropic columnar-grain films on soft (yielding) substrates, but we ignore these special cases here.

The locations of the crack systems in Fig. 1 can be rationalized by stress analysis using FEA. For this we use a contact algorithm described in previous studies.[8,13] A frictionless tungsten carbide (WC) sphere of specified radius r is pressed with incrementally increasing load P onto the top surface of a bilayer with well-bonded isotropic and homogeneous coating and substrate layers. Grid elements are refined until convergence is obtained in dummy runs. Our specific interest here is in the radially directed tensile stresses normal to incipient ring cracks at the top surface and radial cracks at the bottom surface. Pertinent properties of the material systems considered are given in Table I.

Accordingly, Fig. 2 shows radial stress contours, normalized to mean contact pressure $P/\pi a^2$ in accordance with geometrical similarity, corresponding to the four cases illustrated in Fig. 1. The calculations are for glass on polycarbonate but are representative of a range of ceramic/polymer bilayers. In general, there are two tensile stress maxima on each of the coating surfaces, consistent with the crack locations in Fig. 1: on the top surface, at the contact circle and in the outer shoulder

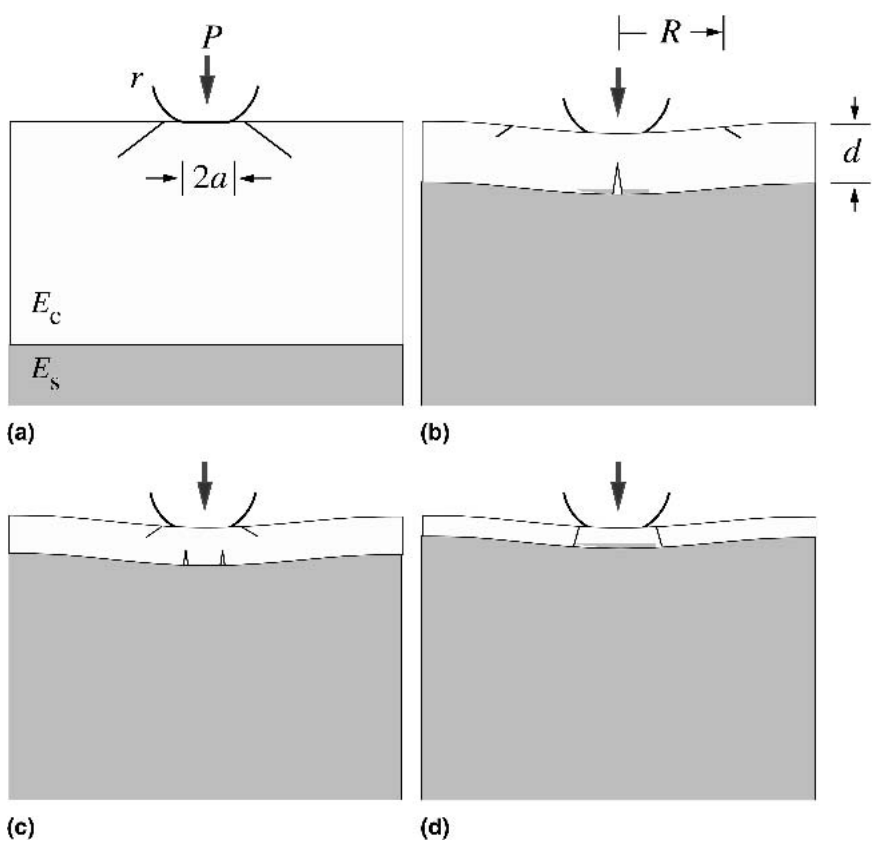

FIG. 1. Schematic illustration of bilayer structure consisting of outer brittle layer of thickness d and modulus E_c on thick compliant substrate of modulus E_s, in axisymmetric contact with sphere of radius r at load P over a circular area of radius a. Fracture mode transitions in brittle layer: (a) cone crack at top surface, (b, c) ring crack at top surface and radial crack at bottom surface, and (d) through-thickness ring cracks.

TABLE I. Mechanical properties for constituent layer and indenter materials.[a]

Material	Young's modulus E (GPa)	Strength S (MPa)	Toughness T (MPa m$^{1/2}$)	Flaw size[b] c_f (μm)
Soda-lime glass	70	110 ± 9	0.67	11.8
Alumina (AD995)	370	570 ± 63	3.1	9.4
Zirconia (Y-TZP)	205	1450 ± 250	5.4	4.4
Polycarbonate	2.3			
Tungsten carbide	614			

[a]Data from Ref. 15. Poisson's ratio for the glass and ceramic coatings taken as $\nu_c = 0.22$, for polycarbonate $\nu_s = 0.35$.
[b]Flaw size c_f estimated from Griffith relation $S = T/\psi c_f^{1/2}$, where T is toughness and $\psi = \pi^{1/2}$ (assuming pennylike flaws).[27]

region; on the bottom surface, at the contact axis and just inside the contact. Figure 2(a), $d/a = 10$, shows a classical Hertzian-like field with primary maximum concentrated at the contact edge, similar to that in a monolith. Figure 2(b), $d/a = 1$, shows a primary maximum at the center bottom surface and a secondary outer maximum at the top surface. Note that the stresses are compressive on the top surface in the vicinity of the contact circle in this case. This stress state is consistent with a dominant flexural stressing mode.[8] Figure 2(c), $d/a = 0.1$, shows similar, near-equal maxima but with an outward shift at the bottom surface and inward shift at the top surface, toward the contact circle. In this case, the tensile stresses at the center lower surface are diminished and laterally diffused by the expanding contact. Figure 2(d), $d/a = 0.04$, shows maxima at the top and bottom surfaces in the near-contact region, indicating the beginnings of a transition to a membrane configuration. The stresses at the center lower surface are now completely compressive. In this last case the substrate carries much of the load, and thereby controls the stress level in the coating. A feature of the stress distributions is the extremely high stress gradients in some of the maxima, especially in the vicinity of the contact circle. High stress gradients are a well-documented feature of contact fields and ultimately bear on the validity of any critical stress criterion for crack initiation.[21,22]

With this background, we are positioned to derive analytical relations for the critical loads to initiate each fracture mode in the different thickness regions. We do this in the subsections below for bottom-surface radial cracks and top-surface ring cracks. For simplicity, we first treat the simple case of a non-expanding contact radius a (punch), followed by the more complex case of an expanding contact from a spherical indenter of radius r (Hertz). It is assumed that fracture initiates when the maximum tensile stress exceeds the bulk strength of the material, and that in any given thickness region, one or other of the contact or plate flexure stress states dominates.

B. Bottom-surface radial cracks

Bottom-surface radial cracks are primary in the intermediate thickness region (region b in Figs. 1 and 2). Here d/a is assumed to be sufficiently small that flexure dominates contact stresses, yet sufficiently large that the load may be represented by a concentrated force. Then the maximum tensile stresses at the center lower coating surface can be obtained from the theory of plates on soft foundations[23]

$$\sigma_c = (P/Bd^2)\log(CE_c/E_s) \quad , \tag{1}$$

with dimensionless coefficients $B = 1.35$ and $C = 1.00$.[24] Equating σ_c in Eq. (1) to the bulk strength S_c of the coating yields the critical load $P = P_{rad}$ for radial cracking

$$P_{rad} = BS_c d^2/\log(CE_c/E_s) \quad . \tag{2}$$

Important dependencies in this relation are quadratic thickness and linear strength. Modulus mismatch, with its logarithmic dependence, is a weaker factor.

In practice, the d^2 dependence is not universally exact, and deviations occur when d/a diminishes below unity, i.e., as the contact engulfs the coating/substrate surface and the radial crack moves laterally outward (region c in Figs. 1 and 2).[17,24] In this region Eq. (1) may be expected to overestimate the tensile stress σ_c, so that P_{rad} in Eq. (2) represents a lower bound to the actual critical load. There are further factors that can contribute to increases in P_{rad} as d/a approaches unity, notably stress gradients and flaw statistics. We will return to this issue in Sec. IV.

C. Top-surface ring cracks

Top-surface ring cracks dominate in the extreme large-thickness and small-thickness regions (regions a and d in Figs. 1 and 2); and, in some uncommon cases, even in the intermediate-thickness region, e.g., when the top surface contains relatively large extrinsic flaws.[8] We consider each of these regions in turn below.

1. Thick layers [$d \gg a$, Fig. 1(a)]

The stresses are concentrated at the contact edge ($R/a \sim 1$), so the coating may be treated effectively as a monolith. Stresses within the contact are largely compressive. The maximum tensile stress in the coating surface scales with the contact pressure, and so may be written

$$\sigma_c = P/Aa^2 \quad , \tag{3}$$

where A is a proportionality coefficient. In true Hertzian contact, $A = 2\pi/(1 - 2\nu_c)$.[22,25] Assuming that a critical load $P = P_{ring}$ is obtained when $\sigma_c = S_c$, we have

$$P_{ring} = AS_c a^2 \quad . \tag{4}$$

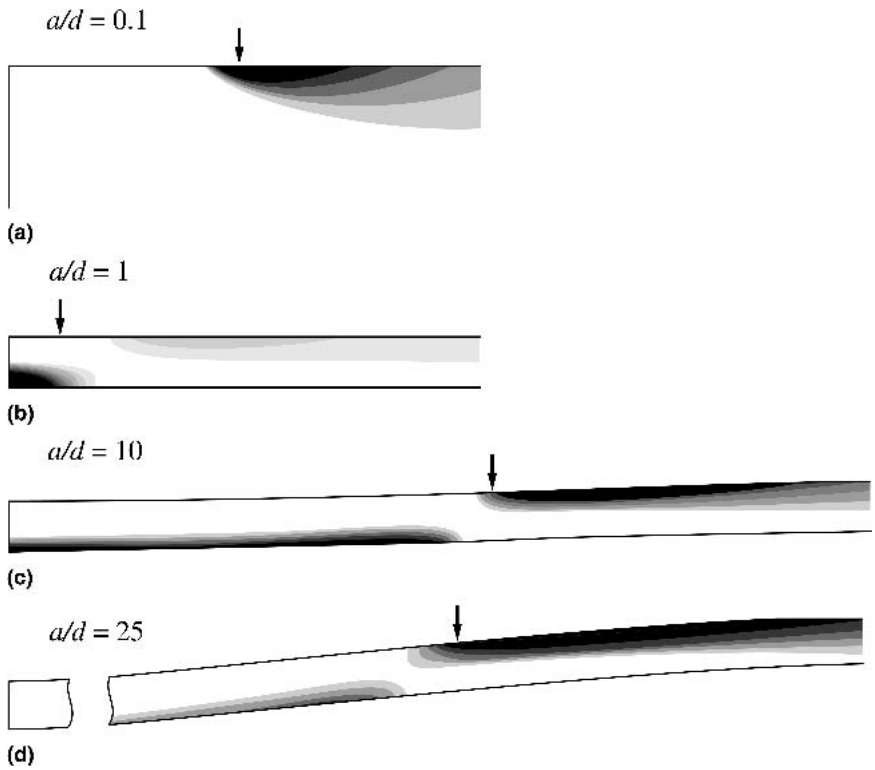

FIG. 2. Contours of radial tensile stresses (shaded areas) in glass plate on polycarbonate substrate, for contact with sphere at top surface. Calculations shown for fixed $d/r = 0.005$, for relative contact radii a/d shown. The left edge of plate corresponds to contact axis; the arrow indicates contact edge. Stresses equispaced in units of mean contact pressure, $p_0 = P/\pi a^2$: white background indicates $p_0 \leqslant 0$ (compression region); black indicates $p_0 \geqslant 1$ (high tension region). Plate thickness in (a) expanded and plate width in (c) sectioned to resolve concentrated stress contours at contact edge. Note large deflections in (d).

Strictly, Eq. (4) holds only in the limit of very small flaw size relative to the contact size ($c_f \ll 0.01a$), where the stress gradients over the flaw depth remain small.[21,22]

Equation (4) is general and holds for either fixed (punch) or expanding (Hertzian) contact. In the latter case it is often preferable to express the critical relations in terms of indenter radius r rather than contact radius a. The Hertzian contact relation for monoliths[25] is

$$a = (KPr/E_c)^{1/3} \quad , \tag{5}$$

with $K = 3(1 - \nu_c^2)/4$. Combination with Eq. (4) leads to an alternative form of the critical load relation

$$P_{ring} = A'(S_c/E_c)^2 S_c r^2 \quad , \tag{6}$$

with $A' = K^2 A^3$.

2. Intermediate layers [$d/a \sim 1$, Fig. 1(b)]

As d/a diminishes toward unity, the tensile stress at the contact circle also begins to diminish. The coating begins to flex and the location of maximum tension at the top surface moves radially outward onto the shoulder [Fig. 2(b)]. The tensile stress may be expected to have a form basically similar to that of Eq. (1), but of lower magnitude. By analogy with Eq. (2) we have[8]

$$P_{ring} = B' S_c d^2/\log(C' E_c/E_s) \quad , \tag{7}$$

at relative radial location

$$R = bd\log(cE_c/E_s) \quad , \tag{8}$$

with coefficients $B' = 45.5$, $C' = 65$, $b = 2.3$, and $c = 1.7$.[17]

Thus $P_{ring} > P_{rad}$ in Eqs. (6) and (7), so that radial cracks are expected to occur before ring cracks in most of the intermediate region. However, this condition may be expected to break down as d/a decreases toward 0.1, where the relative magnitudes of the tensile stresses on the top and bottom surfaces reverse [Fig. 2(c)]. Another exception may occur in cases where the strength of the coating is substantially lower at the top than at the bottom surface (e.g., from preferential abrasion treatment).[8]

3. Thin layers [$d/a \ll 1$, Fig. 1(d)]

In the limit of ultrathin films, the load is essentially supported by the substrate. Then ignoring the coating for the moment, the maximum tensile stress in the substrate at the contact circle has the same form as Eq. (3)

$$\sigma_s = P/Aa^2 \quad , \tag{9}$$

with $A = 2\pi/(1 - 2\nu_s)$. Assuming continuity of strain

across the coating/substrate interface (and similar Poisson's ratio in the two materials), the coating may be considered as a membrane with uniform section stress $\sigma_c = \sigma_s(E_c/E_s)$. Again equating σ_c to S_c, the critical load is

$$P_{\text{ring}} = A(E_s/E_c)S_c a^2 \quad , \tag{10}$$

analogous to Eq. (4) but with a modulus mismatch term included. Actually, as seen in Fig. 2(d), the stresses across the film section are not uniform even at quite low *d/a*, so Eq. (10) again represents a lower bound.

Once more, Eq. (10) may be expressed in terms of indenter radius *r* rather than contact radius *a*. In analogy to Eq. (5), we have

$$a = (KPr/E_s)^{1/3} \quad , \tag{11}$$

with $K = 3(1 - \nu_s^2)/4$. Combining Eq. (10) and (11) yields

$$P_{\text{ring}} = A'(E_s/E_c)(S_c/E_c)^2 S_c r^2 \quad . \tag{12}$$

D. Normalized critical load diagrams

In this subsection, we plot normalized critical loads for top-surface ring or cone cracks and bottom-surface radial cracks as a function of normalized coating thickness, and compare predictions from the relations in Sec. II. B and III. C above with corresponding data from the FEA stress algorithm described in Sec. II. A.

For the first graphical constructions we normalize the critical loads *P* relative to contact radius *a*. In the thick layer region, Eq. (4) reduces to

$$P_{\text{ring}}/S_c a^2 = A \quad . \tag{13}$$

Similarly, in the intermediate layer region, from Eq. (2) and (7)

$$P_{\text{rad}}/S_c a^2 = B(d/a)^2/\log(CE_c/E_s) \quad , \tag{14a}$$

$$P_{\text{ring}}/S_c a^2 = B'(d/a)^2/\log(C'E_c/E_s) \quad . \tag{14b}$$

Finally, in the thin layer region, from Eq. (10)

$$P_{\text{ring}}/S_c a^2 = A(E_s/E_c) \quad . \tag{15}$$

In this scheme, the dimensionless quantity $P/S_c a^2$ is dependent only on relative coating thickness *d/a* and modulus mismatch E_c/E_s, without having to specify strength S_c.

Accordingly, the functional dependence of $P/S_c a^2$ versus *d/a* is plotted in Fig. 3 for three model bilayer systems, glass, alumina and Y-TZP coatings on polycarbonate substrates. The solid lines in these diagrams represent Eqs. (13–15). Data points are corresponding FEA computations—unfilled symbols for top-surface ring cracks and filled symbols for bottom-surface radial cracks—for various combinations of *d* and *r*. The FEA data for each material appear to fall on universal curves, although there are material–material shifts because of the modulus mismatch dependencies. Equations (13–15) provide a useful

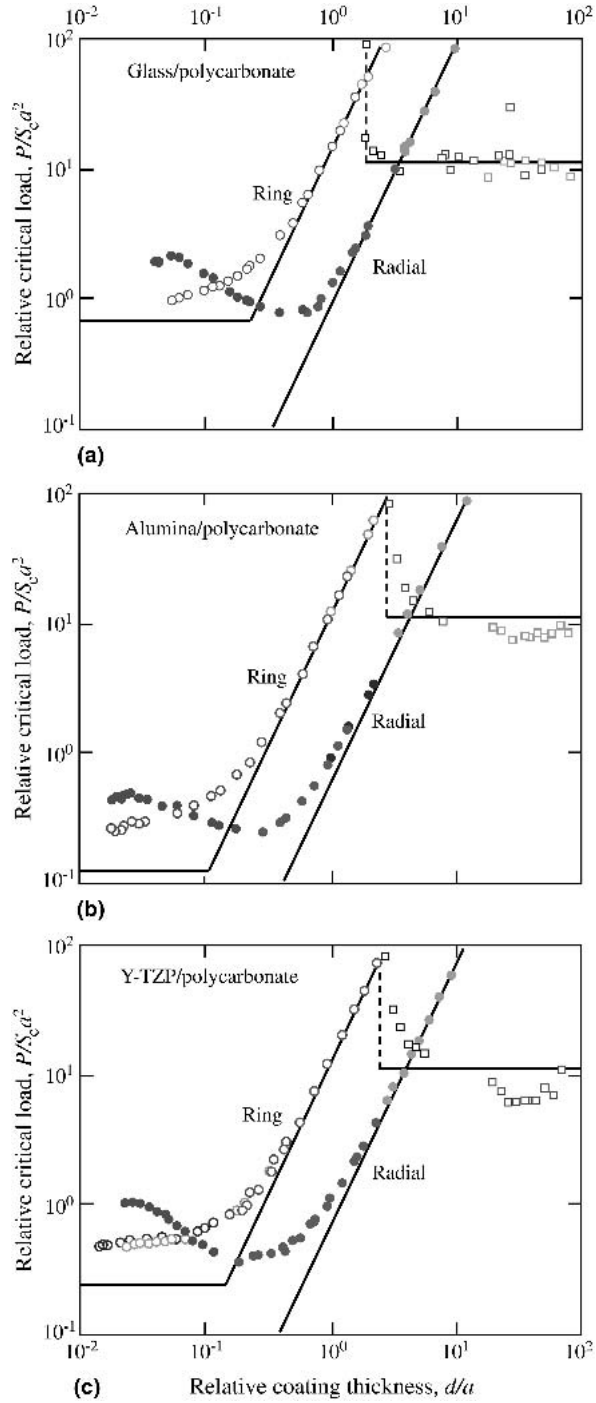

FIG. 3. Plot of normalized critical load $P/S_c a^2$ versus *d/a* for (a) glass, (b) alumina, and (c) Y-TZP coatings on polycarbonate substrates. Solid lines are calculated from Eqs. (13–15). Data points are FEA computations—surface ring cracks (unfilled circles and squares) and subsurface radial cracks (filled circles). (Squares are used to distinguish cone cracks in the large *d/a* region from ring cracks in the intermediate and small *d/a* regions.) Different colored symbols are for different combinations of *d* (3 μm to 3 mm) and *r* (0.86–5 mm).

lower bound to the FEA data, and fit the data asymptotically in the upper intermediate region $1 < d/a < 10$. Of particular note is the upturn in the FEA data for the radial cracks at $d/a < 0.5$, corresponding to configurations where the Hertzian compression field begins to engulf the coating lower surface. The ring crack data show upward deviations in the transition regions. These transition regions may be delineated by the data crossover points $P_{\mathrm{ring}} = P_{\mathrm{rad}}$ at $d/a \approx 3$ (thick–intermediate) and $d/a \approx 0.1$ (intermediate–thin). The FEA data in the region $d/a < 0.1$ approach the asymptotic lower bound more slowly in the alumina and Y-TZP ceramics relative to glass, suggesting that the membrane approximation is less valid in bilayer systems with greater modulus mismatch E_c/E_s.

Figure 4 shows radial location R/a versus d/a for the same three coating systems on a composite plot. Points are FEA data, again with unfilled symbols for top-surface ring cracks and filled symbols for bottom-surface radial cracks. Solid lines in the intermediate thickness region are representations of Eq. (8). This figure quantifies the shifts in ring and radial crack locations with coating thickness, in accordance with Figs. 1 and 2. Note especially the abrupt shifts of the ring crack location at $d/a \approx 3$ and the radial crack at $d/a \approx 0.3$.

The critical loads may similarly be normalized relative to sphere radius r. In the thick layer region, Eq. (6) reduces to

$$P_{\mathrm{ring}} E_c^{\,2}/S_c^{\,3} r^2 = A' \quad . \tag{16}$$

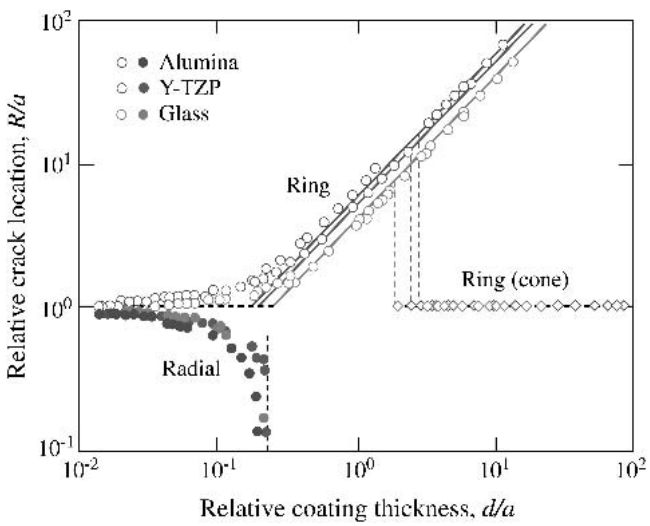

FIG. 4. Composite plot of R/a versus d/a for glass, alumina and Y-TZP coatings on polycarbonate substrates, indicating how the crack locations shift with changing coating thickness. Points are FEA data, surface ring crack (unfilled circles and squares) and subsurface radial cracks (filled circles). Solid lines in the intermediate thickness region are predictions from Eq. (8), horizontal dashed lines indicate location of contact circle ($R/a = 1$). At left of vertical dashed line at $d/a \approx 3$, ring crack location shifts abruptly from near-contact to remote radial location. Similarly, at left of vertical dashed line at $d/a \approx 0.3$, radial crack location shifts abruptly from contact axis ($R/a = 0$, not shown) to near-contact.

In the intermediate layer region, Eqs. (2) and (7) become

$$P_{\mathrm{rad}} E_c^{\,2}/S_c^{\,3} r^2 = B(E_c d/S_c r)^2/\log(C E_c/E_s) \quad , \tag{17a}$$

$$P_{\mathrm{ring}} E_c^{\,2}/S_c^{\,3} r^2 = B'(E_c d/S_c r)^2/\log(C' E_c/E_s) \quad . \tag{17b}$$

In the thin layer region, from Eq. (12)

$$P_{\mathrm{ring}} E_c^{\,2}/S_c^{\,3} r^2 = A'(E_s/E_c) \quad . \tag{18}$$

Again, in this normalization scheme, the dimensionless quantity $P_{\mathrm{ring}} E_c^{\,2}/S_c^{\,3} r^2$ is dependent only on reduced coating thickness $E_c d/S_c r$ and modulus mismatch E_c/E_s.

The functional dependence of $P E_c^{\,2}/S_c^{\,3} r^2$ versus $E_c d/S_c r$ is plotted in Fig. 5 for the same three model bilayer systems as in Fig. 3. Solid lines are Eqs. (16–18), data points are FEA computations. Again, the FEA data for each material appear to fall on universal curves, with material–material modulus mismatch shifts. As before, the simple relations provide lower bounds to the FEA data, although the transition regions in these plots are comparatively abrupt; note especially the near-universal radial-crack transition from intermediate- to thin-layer region at $E_c d/S_c r \approx 2$.

III. EXPERIMENTAL

A. Fabrication and testing of ceramic-coating systems

Tests to validate the theoretical predictions experiments were made on model bilayers fabricated as brittle coatings on polycarbonate substrates, consistent with the systems considered in Figs. 3–5. Thus, starting materials for the coatings included soda-lime glass microscope slides (Fisher Premium, Fisher Scientific, Pittsburgh, PA) and plates, alumina plates (Procera, Nobel Biocare, Göteborg, Sweden) and Y-TZP plates (Prozyr, Norton Desmarquest Fine Ceramics, East Granby, CT). Whereas the glass is homogeneous, the alumina and Y-TZP ceramics have polycrystalline microstructures with equiaxed grains of characteristic dimensions 0.5 and 5 μm, respectively.[26] These model bilayer systems have been tried and tested in past studies, specifically over a coating thickness range 10 mm to 100 μm;[8,10,14] the focus here is on extension of the data range to smaller thicknesses, to investigate more closely the lower transition region [Figs. 1(c) and 1(d)].

Accordingly, coating layers 25 × 25 mm in lateral dimensions were cut from the supplied ceramic plates and ground and polished on both sides (1 μm finish) to prescribed thicknesses within the range $d = 10$ mm to 10 μm. In the case of glass, thinning was accomplished by dissolution in a dilute HF solution, and both top and bottom etched surfaces were then abraded with a SiC slurry (600 grit) to produce a relatively uniform distri-

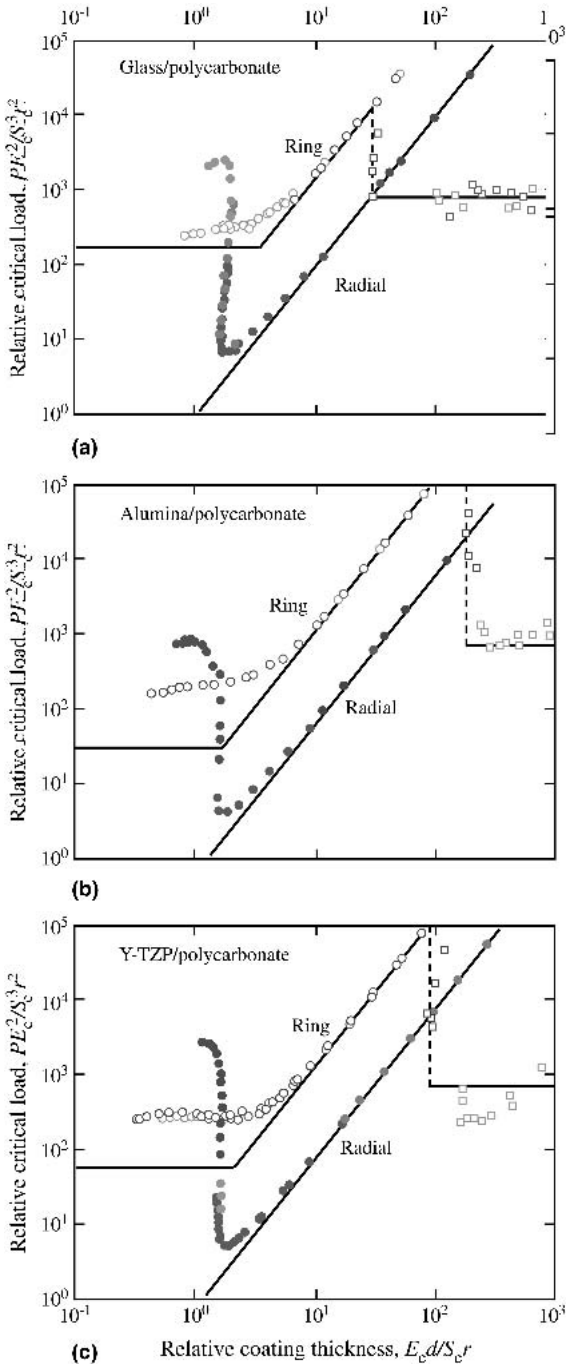

FIG. 5. Plot of normalized critical load $PE_c^2/S_c^3r^2$ versus E_cd/S_cr for (a) glass, (b) alumina, and (c) Y-TZP coatings on polycarbonate substrates. Solid lines are calculated from Eqs. (16–18). Points are FEA data, surface ring crack (unfilled circles and squares) and subsurface radial cracks (filled circles). (Squares are used to distinguish cone cracks in the large *d/a* region from ring cracks in the intermediate and small *d/a* regions.) Different symbols are for different combinations of *d* (3 μm to 3 mm) and *r* (0.86–5 mm).

bution of extrinsic flaws for radial crack initiation.[8] A unique advantage of working with a homogeneous material like glass is the capacity to abrade the top or bottom surface selectively, thus controlling the source of fracture, i.e., either top-surface rings or bottom-surface radials. In alumina and Y-TZP the microstructure ensures a population of intrinsic flaws, so the surfaces of these materials were tested in the as-polished state. The strength values and corresponding calculated flaw sizes[27] in Table I relate to these preparation conditions. The small flaw size in Y-TZP relative to alumina is commensurate with the grain sizes indicated above.

The resulting ceramic layers were bonded to polycarbonate substrates 12.5 mm thick using a thin layer (<20 μm) of epoxy adhesive (Harcos Chemicals, Bellesville, NJ).[8] Because the modulus of the adhesive is similar to that of the substrate material, the adhered system may be regarded effectively as a ceramic/polycarbonate bilayer. Concentrated loads were delivered to the bilayer top surfaces using WC spherical indenters in the radius range $r = 0.86$ to 12.7 mm mounted into the crosshead of a mechanical testing machine (Model 5500, Instron, Corp, Canton, MA). The bottom surfaces of the ceramic plates were viewed in situ through the polycarbonate substrate from below the contact using a video camcorder (Canon XL1, Canon, Lake Success, NY) with a microscope zoom (Optem, Santa Clara, CA). This enabled directed monitoring of initiation of bottom-surface radial cracks, and for very thin ceramic coatings, even top-surface ring cracks. For thicker alumina and Y-TZP coatings, the top surfaces were simply inspected for ring cracking after indentation.[10]

B. Results and analysis

Experimentally determined critical loads P_{rad} and P_{ring} for first fracture are plotted for glass, alumina, and Y-TZP coatings on polycarbonate substrates as a function of coating thickness *d* for specified sphere radii *r* in Fig. 6. Unfilled symbols indicate top-surface ring cracks, and filled symbols indicate bottom-surface radial cracks. The lower limits in the latter data represent the thinnest coatings for which radial cracks were observed. In this region, the crack configuration undergoes a distinctive transition from radial to ring, resulting in the kind of "soccer ball" pattern shown in Fig. 7. The solid curves in Fig. 6 are first-fracture envelopes from spline fits to the corresponding FEA data in Fig. 5, using material parameters in Table I to convert from normalized to absolute coordinates. In the special case of glass [Fig. 5(a)], first-fracture ring-crack data in the intermediate region (dashed curve) are obtained by preferentially abrading the top-surface while leaving the bottom surface in its as-etched state.[8]

The bulk of the data in Fig. 6 lie within the intermediate thickness region of dominant bottom-surface radial cracking, with a few data points extending either side into the domains of dominant top-surface ring-cracking. In our experiments, a special effort was made to reduce coating thicknesses down to a level below which radial cracks no longer initiated. {In the case of Y-TZP [Fig. 6(c)],

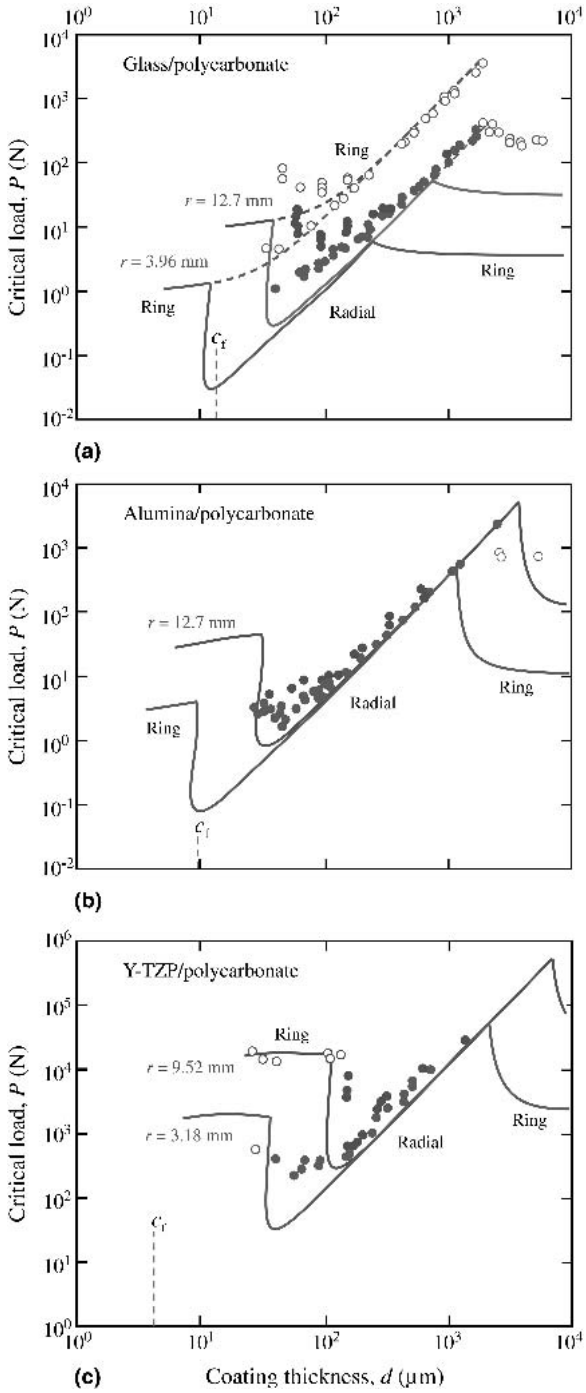

FIG. 6. Experimental data plot of critical loads P_{ring} and P_{rad} versus thickness d for (a) glass, (b) alumina, and (c) Y-TZP coatings on polycarbonate substrates, for sphere radii r indicated. Surface ring cracks (unfilled symbols) and subsurface radial cracks (filled symbols). Solid and dashed curves are from fits to FEA data in Fig. 5. Vertical dashed lines are estimated flaw sizes c_f from Table I. Note different load scale in (c).

no cone crack data are shown in the region $d > 1$ mm because top-surface damage in thick specimens is dominated by quasiplasticity in this relatively soft ceramic.[10,28]} Considering the radial crack first, the experimental data reasonably overlap the FEA (and analytical, Fig. 5) predictions in the upper intermediate region but exhibit enhanced upward deviations and premature cutoffs in the lower intermediate region, the more so for smaller sphere radii. The premature cutoffs are most pronounced in the glass and alumina, and least in the Y-TZP. As to the ring cracks, the data in the thick coating region (where available) lie substantially above the FEA predictions, confirming that the critical stress condition is not an accurate predictor of fracture in this region of high stress gradients. A consequence of this deviant behavior is an effective expansion of the upper intermediate region, somewhat negating the premature cutoffs in the lower intermediate region.

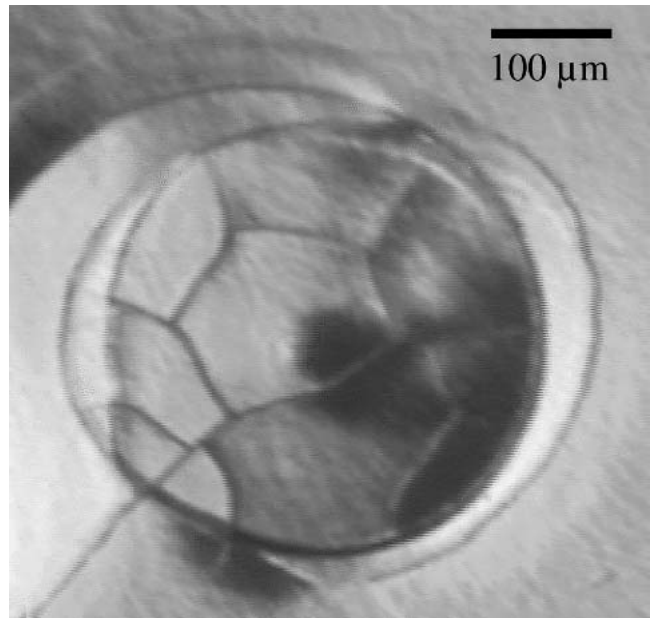

FIG. 7. "Soccer ball" crack pattern in Y–TZP coating of thickness $d = 27$ μm on polycarbonate from contact with WC sphere, $r = 1.57$ mm. Micrograph is frame from video sequence, taken after unloading from $P = 57$ N. Pattern shows linkage of off-center radial cracks, with circumscribed ring cracks. Configuration represents transition between well-defined radial and ring cracking in intermediate and thin coating regions, respectively.

IV. DISCUSSION

We have studied the competition between fracture modes associated with contact loading of brittle coating layers on compliant substrates as a function of diminishing layer thickness d. Two principal modes of fracture operate in such systems: ring cracking at the coating top surface, from near-contact stresses; and radial cracking at the coating bottom surface, from plate flexure stresses. Ring (or cone) cracking dominates in the extreme regions of very large d and very small d, radial cracking in the region of intermediate d. Delamination fractures are not observed, indicating sufficiently strong epoxy bonding between the coating and substrate layers in our systems.

The theoretical treatment in Sec. II yields explicit analytical relations for critical loads for the two cracking modes based on several assumptions: linear elasticity in the stress fields up to the critical load for first fracture—a totally dominant Hertzian contact or point-load layer flexure field in each coating thickness region—and the onset of fracture when the maximum tensile stress equals the bulk strength of the coating material. The analytical relations identify coating thickness, relative to contact or sphere radius, as the important geometrical variable. They also identify controlling material variables, principally coating strength and coating/substrate elastic modulus mismatch. FEA calculations, based on the same assumptions, indicate somewhat higher values for the critical loads in Figs. 3 and 5, especially in the transition domains. Part of the reason for these deviations is a breakdown in the assumption of totally dominant contact or flexural fields; in reality, the energy from the external loading is partitioned between these two fields, resulting in lower tensile stresses and hence higher critical loads in the transition domains. We have also indicated how engulfment of the coating undersurface by the expanding contact field further exacerbates these deviations in the lower intermediate region. Nevertheless, while far from exact over the entire thickness spectrum, the simple analytical relations may be seen as a sound basis for conservative design, and highlight the dangers of simple extrapolation of macroscopic data into the domain of ultrathin films.

Of particular note in the FEA analysis is the near-universal radial-crack transition from intermediate- to thin-layer region at $d/r \approx 2S_c/E_c$ in Fig. 5. Typically, values of S_c/E_c are in the order of 0.005 (e.g., Table I), so the thin-layer region where ring cracks once again dominate radial cracks may be loosely defined by the condition $d < 0.01r$. For contacts of effective sphere radius $r \approx 25$ μm say, as in some nanoindenters, this would correspond to $d < 250$ nm, the domain of ultrathin films.

The experimental radial crack data in Fig. 6 show yet further deviations toward higher critical loads and more abrupt cutoffs relative to the theoretical predictions. The ring crack data show especially pronounced upward deviations in the thick-layer region. Repeated mention has been made of the breakdown of the critical-stress fracture condition as a potential cause of this behavior. The importance of stress gradient effects in the mechanics of crack initiation in near-contact fields has been well documented, for both ring cracking[21,29] and radial cracking.[30] As either contact radius a or coating thickness d diminishes relative to flaw size c_f, typically such that $c_f/a > 0.01$ for ring cracks or $c_f/d > 0.1$ for radial cracks, the average tensile stress over the flaw area progressively decreases below its surface maximum value σ_m. The term $F(c)$ in the stress-intensity factor $K(c) = \sigma_m c^{1/2} F(c)$ for the flaw correspondingly decreases below unity, in which case the critical stress condition $\sigma_m = S$ no longer remains strictly valid. According to this account, deviations and premature cutoffs in the experimental data should be greater for materials with larger c_f, as is indeed the case in Fig. 6, i.e., most pronounced in the glass and alumina, least in the Y-TZP.

Another factor contributing to deviant behavior relates to flaw statistics. The spatial scale of the stress fields diminishes with decreasing d, making it harder to locate large flaws in the vicinity of the maximum stresses and thereby increasing the critical loads.[31,32] Yield in the substrate material can have an opposite effect on the data shifts in the small d region by enhancing plate flexure, especially in stiffer but softer (e.g., metal) substrates.[9–11] In the case of more compliant (e.g., polymeric) substrates, substrate yield can inhibit ring cracking somewhat in the region of very thin coatings.[6] Rate effects from slow crack growth can reduce critical loads.[33] These factors, plus the increasing tendencies to nonlinearities associated with large surface deflections in the thin film region of large a/d [e.g., Figure 2(d)][34] or breakdown in the Hertzian relations at large a/r,[35] can limit the accuracy of any linear analysis. Still other factors—indenter shape, contact friction[9,35]—can further modify near-contact stresses. In such complex cases, well-posed FEA analysis may be regarded as more practical than the simple analytical relations presented here, although at the expense of considerable physical insight into geometrical and material dependencies.

There are additional factors that warrant consideration as coating thicknesses progressively diminish from the thick coating to the ultrathin film domains. It is implicit in our analysis that material properties remain the same at all scales. In our model experiments we have orchestrated this by preparing each set of coatings from the same starting materials, with the same surface preparations, across the thickness spectrum. However, in practical systems, the processing of thin films is generally more refined than that of thick coatings, with consequently smaller grain, and hence flaw, sizes. Thus we may expect the strength S_c, and perhaps even modulus E_c, to increase with decreasing thickness d. The microstructures may also be quite different, e.g., with highly anisotropic columnar grains in thin films formed by vapor deposition. Such films tend to fracture by different modes, i.e., as punch-in failures along the weak columnar interfaces, with substrate yield and attendant delamination cracks.[6]

Finally, a comment is in order concerning the potential use of the simple relations in Sec. II to deconvolute strengths S_c of thin coatings from the critical fracture loads P_{ring} or P_{rad}. Such strength measurements are notoriously difficult to make in real coating/substrate structures. Note has been made above of the many potential sources of deviation between these relations and experi-

mental data. The best agreement between data and prediction is found for radial cracking in the upper intermediate region, suggesting that measurement of critical loads P_{rad} in this region offers the potential for the most reliable evaluations. This would require appropriate scaling of the indenter radius to accommodate the prescribed coating thickness. It may be argued that any such evaluations from critical load data, regardless of the thickness region, pertain more closely to the "effective" strengths of real coating systems, and are to be preferred to estimates from measurements on bulk or free-standing specimens.

ACKNOWLEDGMENTS

This study was supported by National Institute of Standards and Technology (NIST) internal funds. Information of product names and suppliers in this paper is not to imply endorsement by NIST.

REFERENCES

1. D.F. Diao, K. Kato, and K. Hokkirigawa: Fracture Mechanisms of Ceramic Coatings in Indentation. *Trans ASME J. Tribology* **116,** 860 (1994).
2. E. Weppelmann and M.V. Swain: Investigation of the Stresses and Stress Intensity Factors Responsible for Fracture of Thin Protective Films during Ultra-Micro Indentation Tests with Spherical Indenters. *Thin Solid Films* **286,** 111 (1996).
3. L. An, H.M. Chan, N.P. Padture, and B.R. Lawn: Damage-Resistant Alumina-Based Layer Composites. *J. Mater. Res.* **11,** 204 (1996).
4. K. Hayashi and F. Yuan: Elastic-Plastic Analysis of Stresses and Initiation of Cracks in a Ceramic Coating under Indentation by an Elastic Sphere. *ASME J. Tribology* **120,** 463 (1998).
5. J.S. Wang, Y. Sugimura, A.G. Evans, and W.K. Tredway: The Mechanical Performance of DLC Films on Steel Substrates. *Thin Solid Films* **325,** 163 (1998).
6. R. Anderson, G. Toth, L. Gan, and M.V. Swain: Indentation Response and Cracking of Sub-Micron Silica Films on a Polymeric Substrate. *Eng. Fract. Mech.* **61,** 93 (1998).
7. S.V. Hainsworth, M.R. McGurk, and T.F. Page: The Effect of Coating Cracking on the Indentation Response of Thin Hard-Coated Systems. *Surf. Coat. Technol.* **102,** 97 (1998).
8. H. Chai, B.R. Lawn, and S. Wuttiphan: Fracture Modes in Brittle Coatings with Large Interlayer Modulus Mismatch. *J. Mater. Res.* **14,** 3805 (1999).
9. M.R. Begley, A.G. Evans, and J.W. Hutchinson: Spherical Indentation of Thin Elastic Films on Elastic–Plastic Substrates. *Int. J. Solids Struct.* **36,** 2773 (1999).
10. Y-W. Rhee, H-W. Kim, Y. Deng, and B.R. Lawn: Contact-Induced Damage in Ceramic Coatings on Compliant Substrates: Fracture Mechanics and Design. *J. Am. Ceram. Soc.* **84,** 1066 (2001).
11. H. Zhao, X. Hu, M.B. Bush, and B.R. Lawn: Cracking of Porcelain Coatings Bonded to Metal Substrates of Different Modulus and Hardness. *J. Mater. Res.* **16,** 1471 (2001).
12. R.M. Souza, A. Sinatora, G.G.W. Mustoe, and J.J. Moore: Numerical and Experimental Study of the Circular Cracks Observed at the Contact Edges of the Indentations of Coated Systems with Soft Substrates. *Wear* **251,** 1337 (2001).
13. H. Chai and B.R. Lawn: Cracking in Brittle Laminates from Concentrated Loads. *Acta Mater.* **50,** 2613 (2002).
14. Y. Deng, B.R. Lawn, and I.K. Lloyd: Characterization of Damage Modes in Dental Ceramic Bilayer Stuctures. *J. Biomed. Mater. Res.* **63B,** 137 (2002).
15. B.R. Lawn, Y. Deng, P. Miranda, A. Pajares, H. Chai, and D.K. Kim: Overview: Damage in Brittle Layer Structures from Concentrated Loads. *J. Mater. Res.* **17,** 3019 (2002).
16. A. Abdul-Baqi and E.v.d. Giessen: Numerical Analysis of Indentation-Induced Cracking of Brittle Coatings on Ductile Substrates. *Int. J. Solids Struct.* **39,** 1427 (2002).
17. H. Chai: Fracture Mechanics Analysis of Thin Coatings under Spherical Indentation. *Int. J. Fract.* **119,** 263 (2003).
18. V.A. Soloukhin, J.C.M. Brokken-Zijp, and G.D. With: Subsurface Cracking During Indentation on Hybrid Coatings on Polycarbonate. *J. Mater. Res.* **18,** 507 (2003).
19. C-H. Hseuh and P. Miranda: Modeling of Contact-Induced Radial Cracking in Ceramic Bilayer Coatings on Compliant Substrates. *J. Mater. Res.* **18,** 1275 (2003).
20. C-H. Hseuh and P. Miranda: Master Curves for Hertzian Indentation on Coating/Substrate Systems. *J. Mater. Res.* **19,** 94 (2004).
21. F.C. Frank and B.R. Lawn: On the Theory of Hertzian Fracture. *Proc. Roy. Soc. Lond.* **A299,** 291 (1967).
22. B.R. Lawn: Indentation of Ceramics With Spheres: A Century After Hertz. *J. Am. Ceram. Soc.* **81,** 1977 (1998).
23. S. Timoshenko and S. Woinowsky-Krieger: *Theory of Plates and Shells* (McGraw-Hill, New York, 1959).
24. P. Miranda, A. Pajares, F. Guiberteau, Y. Deng, and B.R. Lawn: Designing Damage-Resistant Brittle-Coating Structures: I. Bilayers. *Acta Mater.* **51,** 4347 (2003).
25. K.L. Johnson: *Contact Mechanics* (Cambridge University Press, London, U.K., 1985).
26. Y. Zhang and B.R. Lawn: Long-Term Strength of Ceramics for Biomedical Applications. *J. Biomed. Mater. Res. B.* (in press).
27. B.R. Lawn: *Fracture of Brittle Solids* (Cambridge University Press, Cambridge, U.K., 1993).
28. Y-W. Rhee, H-W. Kim, Y. Deng, and B.R. Lawn: Brittle Fracture Versus Quasiplasticity in Ceramics: A Simple Predictive Index. *J. Am. Ceram. Soc.* **84,** 561 (2001).
29. B.R. Lawn: Hertzian Fracture in Single Crystals with the Diamond Structure. *J. Appl. Phys.* **39,** 4828 (1968).
30. H. Chai: Fracture Mechanics Analysis of Thin Coatings under Plane-Strain Indentation. *Int. J. Solids Struct.* **40,** 591 (2003).
31. F. Guiberteau, N.P. Padture, and B.R. Lawn: Effect of Grain Size on Hertzian Contact in Alumina. *J. Am. Ceram. Soc.* **77,** 1825 (1994).
32. P. Miranda, A. Pajares, F. Guiberteau, F.L. Cumbrera, and B.R. Lawn: Role of Flaw Statistics in Contact Fracture of Brittle Coatings. *Acta Mater.* **49,** 3719 (2001).
33. C-S. Lee, D.K. Kim, J. Sanchez, P. Miranda, A. Pajares, and B.R. Lawn: Rate Effects in Critical Loads for Radial Cracking in Ceramic Coatings. *J. Am. Ceram. Soc.* **85,** 2019 (2002).
34. H-W. Kim, Y. Deng, P. Miranda, A. Pajares, D.K. Kim, H-E. Kim, and B.R. Lawn: Effect of Flaw State on the Strength of Brittle Coatings on Soft Substrates. *J. Am. Ceram. Soc.* **84,** 2377 (2001).
35. K.L. Johnson, J.J. O'Connor, and A.C. Woodward: The Effect of Indenter Elasticity on the Hertzian Fracture of Brittle Materials. *Proc. R. Soc. Lond.* **A334,** 95 (1973).